Vortex simulations of the Rayleigh–Taylor instability

Gregory R. Baker, Daniel I. Meiron, and Steven A. Orszag

Department of Mathematics, Massachusetts Institute of Technology, Cambridge, Massachusetts 02139
(Received 3 December 1979; accepted 9 May 1980)

A vortex technique capable of calculating the Rayleigh–Taylor instability to large amplitudes in inviscid, incompressible, layered flows is introduced. The results show the formation of a steady-state bubble at large times, whose velocity is in agreement with the theory of Birkhoff and Carter. It is shown that the spike acceleration can exceed free fall, as suggested recently by Menikoff and Zemach. Results are also presented for instability at various Atwood ratios and for fluids having several layers.

I. INTRODUCTION

In this paper we describe a very efficient numerical method to study Rayleigh–Taylor instability in inviscid, incompressible, layered flows. The method is an extension of the classical point vortex method.[1] The numerical technique relies on the representation of the density interface by a vortex sheet, i.e., a surface (in two dimensions, a curve) across which the fluid velocity has a continuous normal component, but a discontinuous tangential component; the jump in the tangential velocity is the strength of the vortex sheet. The velocity of the sheet, defined as the average fluid velocity, is given by the Biot–Savart integral in terms of the vortex sheet strength.

Previous numerical computations[1,2] using vortices, on such problems as the roll-up of a vortex sheet behind a wing, the Kelvin–Helmholtz instability, and the development of a Kármán vortex sheet, have run into difficulty at large times. Presumably, this happens because a flow singularity appears after a finite time.[3] For this reason, it is commonly thought that while vortex simulations are useful for obtaining a qualitatively correct picture of the flow, they are not quantitatively reliable. In this paper, it will be shown that in the absence of spontaneous flow singularities, vortex methods can provide accurate and reliable results. The power of these vortex methods lies in their efficiency, flexibility, and ease of implementation.

In Sec. II, we develop the equations of motion of a vortex sheet in a layered fluid, then in Sec. III, we present detailed results for the Rayleigh–Taylor instability of an interface between two fluids. Finally, in Sec. IV we describe several other applications of the present vortex method.

II. VORTEX DYNAMICS IN LAYERED FLOW

In unstratified two-dimensional flow, vorticity is conserved along material paths. In stratified layered flows, vorticity can be produced at density interfaces even in two dimensions, so that an evolution equation for the vortex sheet strength is required. The appropriate equations for a single periodic interface are

$$\frac{d\gamma}{dt} = -\gamma\left(\frac{\partial u}{\partial s}\frac{\partial x}{\partial s}+\frac{\partial v}{\partial s}\frac{\partial y}{\partial s}\right) + 2A\left(g\frac{\partial y}{\partial s}+\frac{\gamma}{4}\frac{\partial \gamma}{\partial s}+\frac{du}{dt}\frac{\partial x}{\partial s}+\frac{dv}{dt}\frac{\partial y}{\partial s}\right), \tag{1}$$

$$2\pi i\frac{d}{dt}(u-iv) = P\int_0^S \frac{d\gamma(s')}{dt}\cot\left(\frac{z(s)-z(s')}{2}\right)ds' - P\int_0^S \frac{\gamma(s')}{2}\left(\frac{dz(s)}{dt}-\frac{dz(s')}{dt}\right) \times \csc^2\left(\frac{z(s)-z(s')}{2}\right)ds', \tag{2}$$

where S is the periodicity interval, P indicates the principal part, γ is the vortex sheet strength, and x and y are the horizontal and vertical components of the position of the sheet parametrized by the arclength s. Also, u and v are the average of the limiting velocity components on each side of the sheet, and g is the acceleration due to gravity directed along the $-y$ axis. Finally, $A=(\rho_2-\rho_1)/(\rho_2+\rho_1)$ is the Atwood ratio where ρ_1 and ρ_2 are the densities of the lower and upper fluids, respectively, and $z=x+iy$.

Equation (1) is obtained by subtracting the tangential component of the momentum equation on one side of the interface from the similar equation on the other side. We use the facts that the pressure is continuous at the interface and the jump in tangential velocity is γ. Equation (2) is the total time derivative of the Biot–Savart law. Further details are given elsewhere.[4]

The total time derivatives in Eqs. (1) and (2) are Lagrangian with respect to the sheet velocity u, v. The first term on the right side of (1) accounts for the changes in vortex sheet strength as the sheet stretches. This is in accordance with conservation of vorticity since points corresponding to fixed values of arclength are not material. The next term on the right side of (1) describes the baroclinic creation of vorticity. There are basically two effects included in this term, namely, the creation of vorticity by gravity and the creation of vorticity by the tangential acceleration of the interface. Note that since u and v are functionally related to γ by the Biot-Savart law (2), Eq. (1) is an integro-differential equation for γ. Equations (1) and (2) correspond closely to equations obtained by boundary-integral methods using dipole source distributions.[5,6]

In the limit of weak stratification and in the absence of initial vorticity, Eq. (1) reduces asymptotically to

$$\frac{d\gamma}{dt} \sim 2Ag\frac{\partial y}{\partial s}. \tag{3}$$

Equation (3) is, in fact, a special form of Bjerknes' theorem.[7] With weak stratification, the Boussinesq ap-

 0031-9171/80/081485-06$00.90

proximation $dp/dy \sim -\frac{1}{2}(\rho_1+\rho_2)g$ implies vorticity production at the rate $\nabla p \times \nabla 1/\rho$ given by Eq. (3). A form of Eq. (3) has been used by Hill[8] to simulate the motion of a buoyant vortex pair.

The numerical calculations with Eqs. (1) and (2) proceed as follows: The vortex sheet is represented initially by a suitable distribution of discrete vortices. The velocity of the sheet is calculated by the Biot–Savart law so that the vortex points may be advanced in time. Next, the change in vortex sheet strength must be calculated. Rather than solving the integro-differential equation directly, which requires an expensive matrix inversion, we use an iteration procedure in which the fluid acceleration at the previous time level is used as a first approximation and then improved.[4,9] For the continuous form of Eqs. (1) and (2), it may be shown that this iteration procedure is globally convergent provided that the interface and vorticity are smooth.[10] For the discrete vortex approximation to Eqs. (1) and (2), convergence is achieved provided there is sufficient spatial resolution. For the calculations reported in this paper, at most three iterations were required to obtain the vortex sheet strength to three significant figures and at most eight iterations were required to obtain eight figures. Finally, the time stepping is done by a fourth-order implicit Adams–Moulton method that requires two evaluations of the time derivatives by the above-described iterative technique each time step.

The vortex method, implemented as above, requires only $O(N)$ computer memory, where N is the number of vortices, and $O(N^2)$ arithmetic operations per time step.

Several other numerical techniques have been used to solve these layered flow problems. Traditional methods based on Green's third formula require $O(N^2)$ computer memory to store a matrix and $O(N^3)$ arithmetic operations to invert the matrix as well as $O(N^2)$ operations (with large coefficient) to set up the coefficients of the matrix. White[11] has used a computer code developed by Hayes[12] to study Rayleigh–Taylor instability with $A=1$ in this way. Longuet-Higgins and Cokelet[13] have used similar methods to study nonlinear surface gravity waves. It seems that with currently available computers, these boundary integral methods are limited to $N \lesssim 150$. For $N \simeq 100$, computer times of the order of 2 sec per time step and computer memory of the order of 50 000 words are typically required by these surface-source integral methods on a CDC 7600 computer. Even with this moderate spatial resolution, our vortex method runs about 10 times faster and requires at least 10 times less memory. However, the vortex calculations can be performed on currently available computers with 1000 or more vortices. Finally, as will be shown in Secs. III and IV and elsewhere for water waves, the vortex calculations are quite accurate even at large surface deformations.

Other techniques to solve these layered flow problems include conformal mapping methods[14,15] and direct numerical solution of the Navier–Stokes equations.[16,17] Conformal mapping seems to work quite well for $A=1$ at moderate surface deformations, but runs into difficulty at large amplitudes for reasons still under study. Operation counts $O(N^2)$ with memory $O(N)$, where N is the surface resolution, can be achieved for moderate deformations.

Direct numerical solution of the Navier–Stokes equations on a two-dimensional $N \times M$ grid in the complex free-surface geometry requires $O(N^a M^b)$ operations with $a+b \gtrsim 3$ (to solve the Poisson equation for the pressure) and $O(NM)$ memory, so such simulations are currently limited to $N, M \lesssim 100$ and are quite costly in computer time.

III. TWO-FLUID RAYLEIGH-TAYLOR INSTABILITY

We apply the vortex method to study the time evolution of an initial disturbance,

$$y = \alpha \cos(2\pi x/\lambda), \tag{4}$$

to an unstably stratified density interface $y=0$ between two fluids at rest. The interface is plotted in Fig. 1 for initial amplitude $\alpha = 0.1\lambda$ and various Atwood ratios A at a time of $(2\lambda/Ag)^{1/2}$. At this time, linear stability theory predicts growth of the interface by a factor $\cosh 2\sqrt{\pi} \simeq 17.3$, independent of A. Observe that the true growth factor in this time interval is about 9.5 for $A=1$, 5.5 for $A=\frac{1}{3}$, and 4.9 for $A=0.1/2.1$, a decreasing function of A.

In Figs. 2 and 3, we plot the amplitude of the bubble at $x=0$ and the spike at $x=\frac{1}{2}\lambda$ as they grow in time for two different Atwood ratios. For comparison we also plot the interface growth as predicted by linear theory, i.e.,

$$y = 0.1\lambda \cosh(2\pi A g/\lambda)^{1/2} t,$$

and the motion of a fluid particle in free fall in a reduced gravity field, i.e., $y = 0.1\lambda + \frac{1}{2}gAt^2$. In all cases the bubble and spike amplitudes grow more slowly than predicted by linear theory. As the Atwood number in-

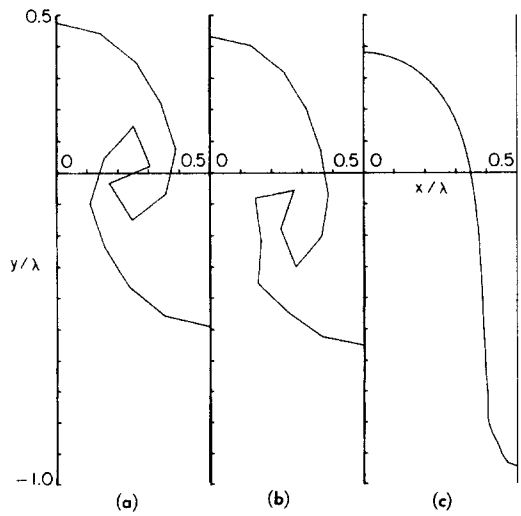

FIG. 1. Profiles of the density interface at time $t=(2\lambda/Ag)^{1/2}$ for various Atwood ratios. The interface is initially perturbed as $y=0.1\lambda \cos(2\pi x/\lambda)$ and the fluids are initially at rest. (a) $A=0.1/2.1$, (b) $A=1/3$, and (c) $A=1$.

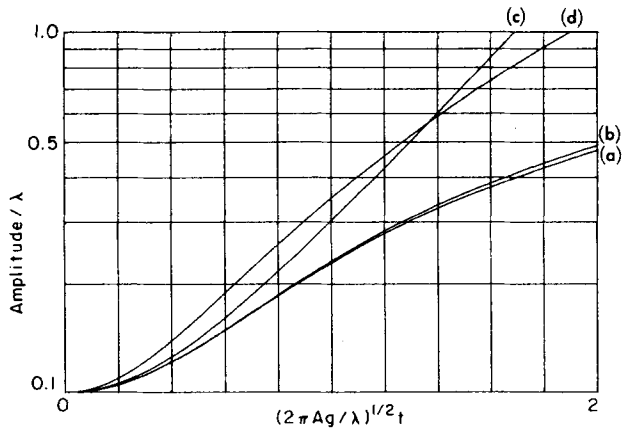

FIG. 2. A plot of the amplitudes of (a) the bubble and (b) the spike as a function of time for various Atwood ratios. Also plotted are (c) the linear growth amplitude and (d) the path of a particle falling freely in the reduced gravity field gA. Here, the Atwood ratio is $A = 0.1/2.1 = 0.048$.

creases, the spike amplitude approaches the linear theory prediction for small times.

For small values of the Atwood ratio, the interface between the fluids begins to roll up due to Helmholtz instability along the vertical vortex sheets (see Fig. 1). At later times, large-scale organized vortex structures should emerge. Since vortex sheet calculations are unreliable for studying vortex sheet roll-up,[1,2] we use only 31 vortices to represent one wavelength. Increasing the number of vortices results in a deterioration of the late-time instability calculation for $A < 1$. In order to obtain even the modest roll-up plotted in Fig. 1, it was necessary to redistribute points equally spaced in arc length.[18] The profiles plotted in Fig. 1 are in qualitative agreement with numerical simulations based on solving the full Navier–Stokes equations.[16,17]

For Atwood ratio 1, in which fluid falls freely into a vacuum, there is no roll-up so increasing the number of vortices leads to an improvement in the description of the sheet. In Fig. 4, we plot the evolution of the sheet with initial condition (4), with $\alpha = 0.5$ and $\lambda = 2\pi$, using 120 vortices and a time step $\Delta t = 0.002(\lambda/g)^{1/2}$ to represent the full wavelength. An ever narrowing

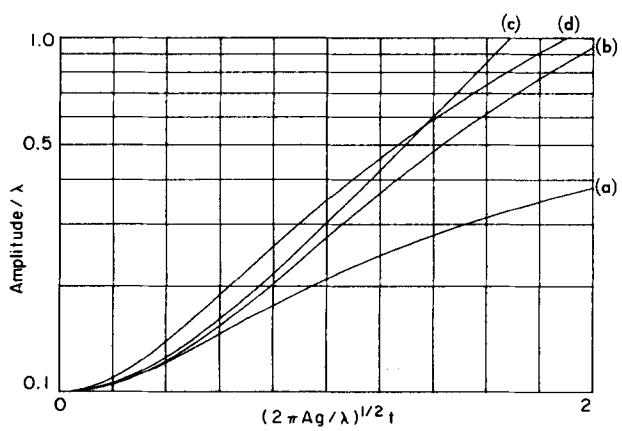

FIG. 3. Same as Fig. 2 except $A = 1$.

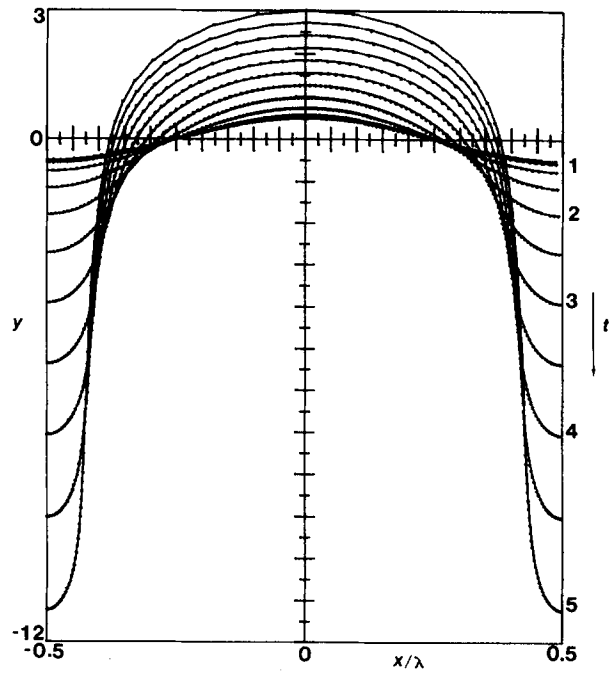

FIG. 4. Plot of the interface $y(x, t)$ at times $t = 0$–5 (0.5). The dots on the interface indicate the position of markers moving with the Lagrangian velocity of the upper fluid. The fluid is initially at rest with the initial interface given by Eq. (4) with $\alpha = 0.5$, $\lambda = 2\pi$. Here $g = 1$ and the Atwood ratio $A = 1$.

spike and broad bubble are seen to develop rapidly. With the Lagrangian scheme described in Sec. II, the vortices move along the interface with a tangential velocity which is the average of the tangential velocities on either side of the interface. Thus, the vortices exhibit a tendency to move away from the developing spike and bubble regions. This effect limits the accuracy attainable on the spike at late times. A better representation is obtained by following the Lagrangian motion of the upper fluid only. In this way, we obtain the accurate, high amplitude results plotted in Fig. 4 in which the spike amplitude is nearly twice the wavelength.

We have compared the accuracy of the results plotted in Fig. 4 with results obtained by the conformal mapping method of Menikoff and Zemach.[15] With initial amplitude $\alpha = 0.5$ and wavelength $\lambda = 2\pi$, the results of the vortex and conformal mapping methods are in complete agreement up to the maximum spike amplitude of about 4 or time $t \simeq 1.2(\lambda/g)^{1/2}$ for which reliable conformal

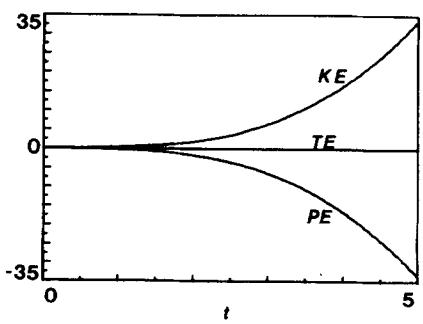

FIG. 5. A plot of the potential (PE), kinetic (KE), and total (TE) energies vs time for the Rayleigh–Taylor instability run plotted in Fig. 4.

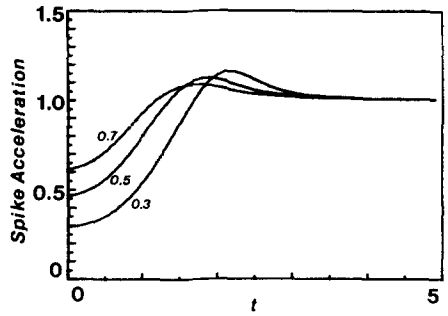

FIG. 6. A plot of normalized acceleration a/g vs time at the tip of the spike for Rayleigh–Taylor instability runs with the fluid initially at rest and the initial interface given by Eq. (4) with $\lambda = 2\pi$, $\alpha = 0.3$, 0.5, and 0.7. Here $g = 1$ and $A = 1$.

mapping results are now available. Comparisons between vortex method results with various numbers of vortices and time steps suggest that the vortex results used to obtain Figs. 4–8 are accurate to at least five significant figures.

A useful diagnostic of the calculation is energy conservation. In Fig. 5, we plot the kinetic, potential, and total energy versus t for the run plotted in Fig. 4. Energy is conserved to better than 1 part in 10^5 at late times. In fact, the kinetic energy at large times is proportional to $(t - t_0)^3$, which follows from a free falling spike of width proportional to $1/(t - t_0)$ and a steady-state bubble, where t_0 is a virtual origin of time that depends on the initial amplitude. For $\alpha = 0.3$, $t_0 \simeq 0.66$; for $\alpha = 0.5$, $t \simeq 0.34$; and for $\alpha = 0.7$, $t_0 \simeq 0.18$.

Our high-resolution vortex calculations with $A = 1$ can be used to resolve some long-standing questions regarding Rayleigh–Taylor instability. In Fig. 6, we plot the acceleration at the tip of the spike ($x = \pm \frac{1}{2}\lambda$) as a function of time t for runs with initial amplitudes $\alpha = 0.3$, 0.5, and 0.7 and wavelength $\lambda = 2\pi$. At late times, the acceleration of the spike approaches the free-fall acceleration g. Shanks transformation[19] of the late-time results gives the extrapolated spike accelerations listed in Table I. Observe that the spike acceleration overshoots g, a feature which is especially pronounced for small initial amplitudes. Menikoff and Zemach (private communication) have observed this phenomenon in their conformal mapping calculations and explain it heuristically as follows: Near the tip of the spike, the flow velocity can be larger on the

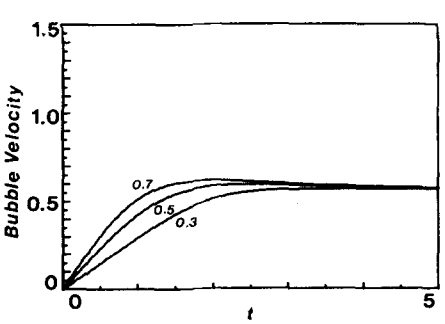

FIG. 7. A plot of the velocity vs time at the peak of the bubble for the same three instability runs as in Fig. 6.

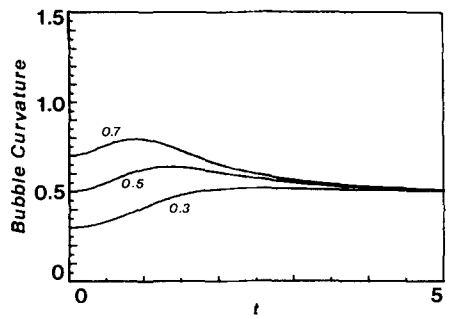

FIG. 8. A plot of curvature κ vs time at the peak of the bubble for the same three instability runs as in Fig. 6.

boundary than on the axes, $x = \pm \frac{1}{2}\lambda$, so the pressure gradient at the tip of the spike can be larger than g.

In Fig. 7, we plot the velocity at the peak of the bubble versus t for initial amplitudes $\alpha = 0.3$, 0.5, and 0.7 and wavelength $\lambda = 2\pi$. At late times, the bubble velocity approaches $0.225\sqrt{g\lambda}$ independent of α. Shanks transformations of the late-time bubble velocity are listed in Table I. In Fig. 8, we plot the curvature κ at the peak of the bubble $x = 0$. At late times, κ approaches $3.1/\lambda$ (see Table I). The results plotted in Figs. 7 and 8 are in agreement with the theory of Birkhoff and Carter,[20] who find a bubble velocity $F\sqrt{g\lambda}$, with Froude number $F = 0.23 \pm 0.01$. Our computed Froude number, 0.225 ± 0.002, of the bubble is somewhat smaller than the lower bound 0.236 suggested by Garabedian[21] on the basis of a stability argument. Our result, $F \simeq 0{:}225$, is in agreement with laboratory measurements[22] that give $F = 0.2$–0.3.

We have also studied the evolution of Rayleigh–Taylor instability with initial surface deformations of the form

$$y = \alpha \cos 2\pi x/\lambda + \beta \cos 2\pi n x/\lambda \tag{5}$$

separating a fluid at rest from a vacuum ($A = 1$). With $\alpha = 0.1\lambda$, $\beta = 0.01\lambda$, $n = 5$, and $\lambda = 2\pi$, a problem previously studied by White,[11] we obtain the results plotted in Fig. 9 using 200 vortices. Observe that the growth of the short wave spike on the long wave bubble is enhanced relative to the growth of the short wave spike on the long wave spike. This follows from the higher effective gravity acting in the bubble region.

At late times, we encountered some difficulty in continuing these calculations due to resolution problems near the short wave spike in the bubble region. It is natural to question whether this difficulty is due merely to resolution or rather to the emergence of a curvature

TABLE I. Shanks extrapolation of large-time spike acceleration, bubble velocity, and bubble curvature for the Rayleigh–Taylor instability of the interface (4) between a vacuum and a fluid initially at rest.

α	Spike acceleration/g	Bubble velocity/$\sqrt{g\lambda}$	$\kappa\lambda$
0.3	1.000 ± 0.002	0.226 ± 0.001	3.14 ± 0.01
0.5	1.000 ± 0.002	0.225 ± 0.001	3.10 ± 0.01
0.7	1.000 ± 0.002	0.225 ± 0.001	3.10 ± 0.01

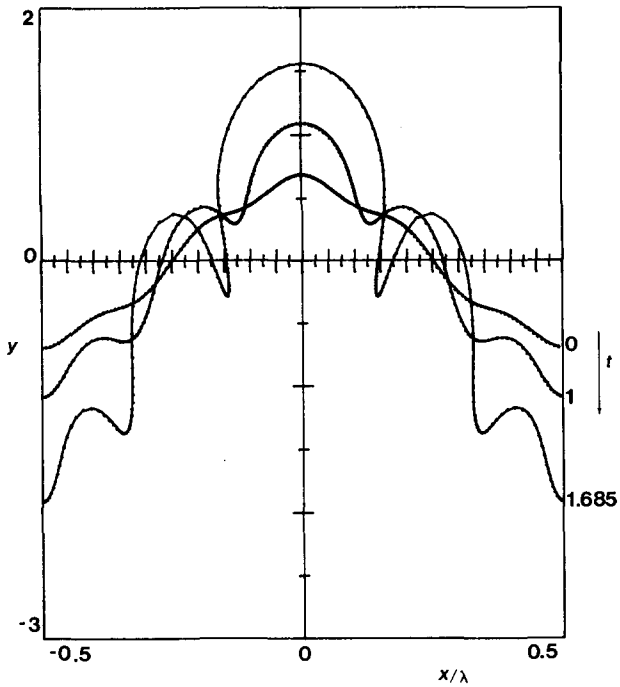

FIG. 9. Profiles of the density interface at times $t=0$, 1.0, and 1.685 for Atwood ratio $A=1$. The interface is initially perturbed as in Eq. (5) with $\alpha=0.1$, $\beta=0.01$, $n=5$, and $\lambda=2\pi$. The fluid is initially at rest and $g=1$.

singularity on the interface at this spike. In Fig. 10, we plot the logarithm of the curvature at this short wave spike versus t while our vortex calculation is demonstrably accurate. There seems to be no tendency for an explosive growth of κ to occur. From these results and similar ones using 100 vortices, we tentatively conclude that a curvature singularity does not appear and that resolution is indeed the problem. Methods to improve the numerical evaluation of the Biot–Savart integral in such short wave spike regions are now under study.

The two-frequency Rayleigh–Taylor instability run plotted in Fig. 9 exhibits some interesting features. First, all three spikes are nearly in free fall by the end of the run. Also, the large bubble (near $x=0$) has achieved a nearly constant velocity of about $0.28\sqrt{g\lambda}$ or $0.71\sqrt{g\kappa}$, where κ is the radius of curvature at the peak of the bubble.

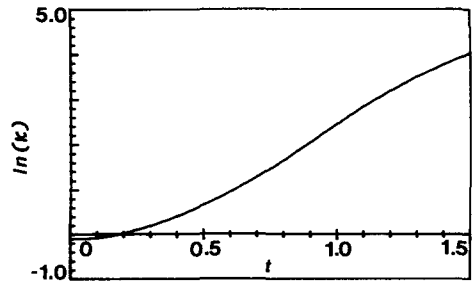

FIG. 10. A plot of the logarithm of the curvature at the tip of the spike nearest the large bubble vs time for the two-frequency instability run plotted in Fig. 9.

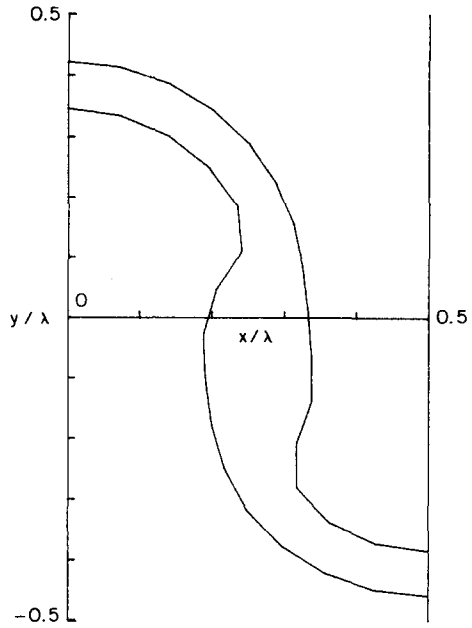

FIG. 11. Profile of the density interface in a three-fluid system at $t=2.22(\lambda/g)^{1/2}$. The densities are 2, $\sqrt{2}$, and 1. The initial disturbance is described in the text.

IV. OTHER APPLICATIONS

In this section, we demonstrate the flexibility of the vortex technique. A simple generalization is the treatment of more than one interface; specifically, Eqs. (2) and (3) are replaced by sums of integrals over all the interfaces. In Fig. 11, we plot the development of Rayleigh–Taylor instability in a three-layer system at a time of $2.22(\lambda/g)^{1/2}$. The two interfaces are specified initially by $0.05\lambda[\cos(2\pi x/\lambda)\pm 1]$ and the three fluids are assumed to have densities of 2, $\sqrt{2}$, and 1. The results show that the upper and lower fluid compress the intermediate fluid layer as they accelerate downward and upward, respectively. The intermediate fluid accumulates where roll-up would occur in a two-layer system with $A=\frac{1}{3}$.

The present techniques should find useful application to the study of instabilities in accelerating and imploding systems, as well as in studies of nonlinear surface and internal waves. Applications of the vortex method to such problems as breaking surface waves, effects of viscosity and surface tension, waves on a beach, and interaction of solid bodies with nonlinear surface and internal waves will be given elsewhere.

ACKNOWLEDGMENTS

We would like to thank Dr. R. L. McCrory, Dr. R. Menikoff, and Dr. C. Zemach for helpful discussions.

This work was supported by the Los Alamos Scientific Laboratory which is supported by the U. S. Department of Energy, by the Office of the Naval Research under Contract No. N00014-77-C-0138, and by the National Science Foundation under Grant ATM-7817092. The high resolution calculations reported in Sec. III were performed at the Computing Facility of the National Center for Atmospheric Research, Boul-

der, Colorado, which is supported by the National Science Foundation.

[1]P. G. Saffman and G. R. Baker, in *Annual Review of Fluid Mechanics* (Annual Reviews, Palo Alto, Calif., 1979), Vol. 11, p. 95.
[2]G. R. Baker, J. Comput. Phys. **31**, 76 (1979).
[3]D. W. Moore, Proc. R. Soc. London Ser. A **365**, 105 (1979).
[4]G. R. Baker and D. I. Meiron, Cambridge Hydrodynamics, Inc. Report No. 36 (1980) (to be published).
[5]G. Birkhoff, Los Alamos Scientific Laboratory Report LA-1862 (1954).
[6]M. A. Jaswon and G. T. Symme, *Integral Equation Methods in Potential Theory and Elastostatics* (Academic, New York, 1977).
[7]H. Lamb, *Hydrodynamics* (Dover, New York, 1932), 6th ed.
[8]F. M. Hill, J. Fluid Mech. **71**, 1 (1975).
[9]S. J. Zaroodny and M. D. Greenberg, J. Comput. Phys. **11**, 440 (1973).
[10]S. Bergman and M. Schiffer, *Kernel Functions and Elliptic Differential Equations in Mathematical Physics* (Academic, New York, 1953), p. 334.
[11]G. N. White, Los Alamos Scientific Laboratory Report LA-5575-MS (1974).
[12]J. K. Hayes, Los Alamos Scientific Laboratory Report LA-4423 (1970).
[13]M. S. Longuet-Higgins and E. D. Cokelet, Proc. R. Soc. London Ser. A **364**, 1 (1978).
[14]D. I. Meiron, S. A. Orszag, and M. Israeli, Cambridge Hydrodynamics, Inc. Report No. 34 (1980) (to be published).
[15]R. Menikoff and C. Zemach, J. Comput. Phys. (to be published).
[16]B. J. Daly, Phys. Fluids **10**, 297 (1967).
[17]D. L. Book, J. P. Boris, M. J. Fritts, R. V. Madala, N. D. Winsor, and S. T. Zalesak, NRL Memorandum Report 4095 (1979), p. 36.
[18]G. R. Baker, J. Fluid Mech. (to be published).
[19]C. M. Bender and S. A. Orszag, *Advanced Mathematical Methods for Scientists and Engineers* (McGraw–Hill, New York, 1978), p. 368.
[20]G. Birkhoff and D. Carter, J. Rat. Math. Mech. **6**, 769 (1957).
[21]P. R. Garabedian, Proc. R. Soc. London Ser. A **241**, 423 (1957).
[22]H. W. Emmons, C. T. Chang, and B. C. Watson, J. Fluid Mech. **7**, 177 (1959).